IEEE Access
Multidisciplinary | Rapid Review | Open Access Journal

Received 10 July 2023, accepted 20 July 2023, date of publication 26 July 2023, date of current version 1 August 2023.

Digital Object Identifier 10.1109/ACCESS.2023.3298628

RESEARCH ARTICLE

Remote Sensing Image Reconstruction Method Based on Parameter Adaptive Dual-Channel Pulse-Coupled Neural Network to Optimize Multiscale Decomposition

PENGCHENG HU[1], SHIHUA TANG[1,2], YAN ZHANG[1], XIAOHUI SONG[1], AND MENGBO SUN[1]

[1]College of Geomatics and Geoinformation, Guilin University of Technology, Guilin 541004, China
[2]Guangxi Key Laboratory of Spatial Information and Geomatics, Guilin 541004, China

Corresponding author: Shihua Tang (2120201690@glut.edu.cn)

This work was supported by the National Natural Science Foundation of China under Grant 41864002, Grant 42261063, and Grant 41901370.

ABSTRACT Existing image processing methods usually divide image denoising and image fusion into two directions for research, and even the best current image denoising methods such as DnCNN can cause information loss during image processing, and the image fusion method mainly considers the fusion between multiple source images to complement the image information, but does not take into account the degradation of the fusion quality due to the noise in the source images. Therefore, aiming at the problem that various existing image denoising methods cannot reduce noise efficiently in complex noise situations while performing multi-source image fusion, preserving texture details, highlighting edge contour structures, and enriching image energy, a method of reconstructing remote sensing images by simplified adaptive dual-channel PCNN (Dual-PCNN) fusion in the NSCT transform domain is proposed to unify image noise reduction and image fusion under the same framework to obtain a noisy image information reconstruction method, which completes the complementary advantages between two image processing methods. Firstly, the impulse noise in the image is removed using IMFLED filtering, and then the Gaussian noise is processed by DnCNN and FFDNet respectively, and the results are imported into simplified parametric adaptive dual-channel PCNN to fuse the preprocessed images respectively. Then the DnCNN image and the preprocessed image are decomposed by NSCT to obtain each low-frequency sub-band and high-frequency sub-band. The low-frequency sub-band is stimulated with detail using the guided filter, and the high-frequency sub-band is enhanced by separating the detail layer through the guided filter to obtain the energy-detail-enhanced high-frequency sub-band. Finally, the corresponding sub-bands are fused into the simplified parametric adaptive dual-channel PCNN respectively, and the fused sub-band coefficients are reconstructed by NSCT inversion to obtain the final reconstructed remote sensing image. The experiments on grayscale images and remote sensing images show that this method achieves excellent results in both visual subjective and quantitative index evaluation, and the reconstructed images perform well in texture details, contour structure, and energy enrichment. After the information reconstruction of remote sensing images, the quality and resolution of remote sensing images are effectively improved, so that terrain information, landform features, and structural features can be extracted more accurately, which are widely used in remote sensing and geographic information fields such as landform analysis, agricultural monitoring, building inspection and environmental protection.

INDEX TERMS Image reconstruction, non-subsampled contourlet transform (NSCT), pulse-coupled neural network (PCNN), convolutional neural network (CNN), guided filter.

I. INTRODUCTION

Optical remote sensing images have the characteristics of low noise and high spatial resolution, and they are widely

The associate editor coordinating the review of this manuscript and approving it for publication was Kumaradevan Punithakumar.

used in the fields of land agriculture and forestry monitoring, urban construction planning, and wetland dynamic change monitoring [1]. Remote sensing images are often subject to external environmental factors and equipment limitations in the process of optical imaging, transmission, and storage, resulting in noise-contaminated images, so it is of certain research value and significance to reconstruct remote sensing images with noise reduction to improve image quality and increase image interpretability when analyzing and interpreting remote sensing images [2].

There are numerous methods for image denoising based on different theories. The reference [3] proposed Block Matching and 3D Filtering (BM3D) image denoising based on Non-local Self Similarity (NSS),, which performs similar block matching group denoising of images by minimum Euclidean distance; the reference [4] used Nuclear Norm Minimization (NNM) instead of low-rank matrix, and image noise reduction by finding the global optimal solution of non-convex optimized low-rank matrix, which has the problem of consistent treatment of singular values; the reference [5] proposed Weighted Nuclear Norm Minimization (WNNM) to choose different weights for singular values, which better recovers the low-rank matrix and has better denoising with better results; in the reference [6], a Denoising Convolutional Neural Network (DnCNN) was proposed, and the network learning object is the image residual; in the reference [7], the Fast and Flexible Denoising Convolutional Neural Network (FFDNet) was proposed on DnCNN basis, and the adaptability to different noises after adding noise levels is higher than that of DnCNN; The reference [8] proposed Wasserstein Generative Adversarial Networks (WGAN) and applied it to cell image denoising to solve the problem of blurred image texture details after CNN denoising, and achieved certain results; the reference [9] used generative adversarial networks and non-residual learning process for blind image denoising application to solve image artifacts and blurring problems; the reference [10] introduced an iterative correction scheme and proposed an effective guided feature domain denoising residual network for real-world noise denoising with some progress. Each theoretical method has different noise reduction effects, but basically, there are problems such as loss of image texture details, blurred edge contour structure, and insufficient image energy.

Image fusion is mainly divided into two categories: spatial domain and transform domain. The main methods in the spatial domain are Principal Component Analysis (PCA) [11] and Gram-Schmidt (GS) [12], whose main feature is to convert the image into a certain feature space for processing, such as color and luminance space. The transform domain method is to reconstruct the decomposed bands by fusing them with relevant rules after transforming the image with multi-scale decomposition. Contourlet Transform (CT) method in reference [13], through the directional anisotropy and local information property of contour wave, solves the problem of poor performance of sub-band directional information and contour structure in image fusion; the reference [14] proposes Non-Subsampled Contourlet Transform (NSCT) based on CT solves the translation invariance while inheriting the advantages of CT; the reference [15] completes the fusion of multimodal medical images by NSCT; the reference [16] fuses two difference remote sensing images by NSCT for natural disaster change detection. Meanwhile, artificial neural networks [17] and convolutional neural networks [18] are also widely used in image fusion to improve image fusion quality.

Pulse Coupled Neural Network (PCNN) [19] is an artificial neural network that can extract image information features without training and is widely used in image fusion, segmentation, and denoising, and its performance is related to the built-in parameters. PCNN can be used for image fusion alone or fused jointly with other algorithms. The reference [20] proposed a simplified parameter adaptive setting method for SPCNN; the reference [21] optimized PCNN based on Multiple Features Grey Wolf Optimizer (MFGWO-PCNN) for multimodal medical image segmentation; the reference [22] proposed an adaptive parametric dual-channel PCNN based on fractal dimension for multifocal image fusion; the reference [23] proposed a parametric adaptive unit-connected dual-channel PCNN for infrared and visible image fusion, incorporating fractal dimension and multiscale morphological gradients into the connection coefficients; the reference [24] proposed a new parametric adaptive unit-connected model (PAULPCNN) for MRI-PET/SPECT medical image fusion; the reference [25] proposed a novel parameter-adaptive dual-channel modified simplified pulse coupled neural network (PA- DC-MSPCNN) for single image dehazing in intelligent transportation systems; the reference [26] proposed a Dual Channel Pulse Coupled Neural Network (DC-PCNN), which is applied to dual-channel parametric adaptive image fusion, but it is less effective for remote sensing image fusion and has serious loss of spatial information.

In summary, image noise reduction and fusion methods are important for reconstructing high-quality remote sensing images from noisy optical remote sensing images [27].

The research work in this article is as follows:

1. This article proposes a simplified parametric adaptive Dual-PCNN fusion model based on DC-PCNN, where the input neuron matrix and Laplace operator do two-dimensional convolution operation to obtain adaptive link strength coefficients, simplify the internal activity terms of neurons, improve computational efficiency, and enhance image feature extraction performance.

2. This article proposes an Iterative Median Filter based on Local Extreme value noise Detection (IMFLED) [28] with DnCNN and FFDNet to jointly reduce impulse and Gaussian mixed noise, and IMFLED-DnCNN and IMFLED-FFDNet multi-source images by simplified parametric adaptive Dual-PCNN fusion to obtain low-noise images. The DnCNN and FFDNet in the framework of this paper are network models trained in advance by the original authors, while the Dual-PCNN in this paper is a non-learning trained

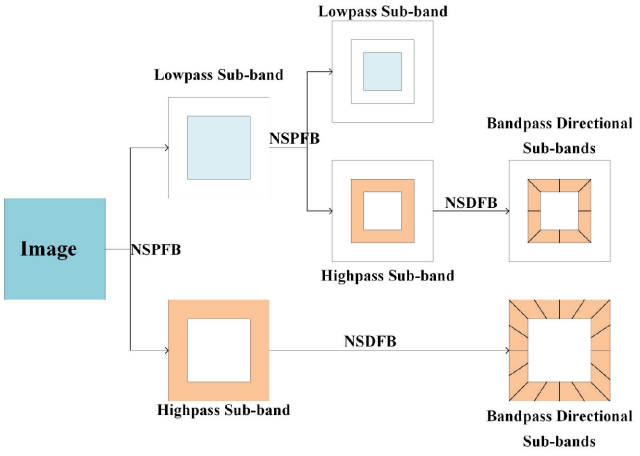

FIGURE 1. The architecture of the NSCT model.

neural network with a single re-run. In this paper, all the modules are integrated under the unified framework.

3. This article design two separate sub-band fusion rules in the NSCT domain. The original low-frequency sub-band is used as the guide image by the guided filter [29] so that the low-frequency sub-band stimulus produces more texture detail information. The guided filter uses the original image as the guided image and decomposes the detail layer after filtering, which is enhanced by the enhancement coefficient and fused with the high-frequency sub-band with high structural similarity so that the contour structure of the high-frequency sub-band is highlighted.

4. The enhanced sub-bands are reconstructed by simplified parametric adaptive Dual-PCNN fusion and the images are reconstructed by NSCT inversion. In order to verify the effectiveness and robustness of the method, the comparison verification experiments are carried out by multiple sets of grayscale images and optical remote sensing images respectively, and the quantitative analysis is performed by using multiple types of evaluation indexes.

The rest of this article is organized as follows. Section II introduces related theories. Section III introduces the research methodology of this article. Section IV extensive grayscale image experiments and optical remote sensing image experiments and ablation experiments are conducted to evaluate this research method. Section V gives some discussions and Section VI gives the conclusion about this article.

II. RELATED THEORIES

A. NON-SUBSAMPLED CONTOURLET TRANSFORM

NSCT has excellent characteristics of multi-scale, multi-direction, and translation invariance for image decomposition. Multi-scale and multi-directional image decomposition is performed by Non-Subsampled Pyramid Filter Banks (NSPFB) and Non-Subsampled Direction Filter Banks (NSDFB). The original image is first decomposed into a low-pass sub-band and a high-pass sub-band by NSPFB, and the high-pass sub-band is decomposed into multiple band-pass direction sub-bands by NSDFB, and then the low-frequency sub-band is decomposed by NSPFB transform, and the process is repeated. The size of each sub-band remains unchanged while decomposing to avoid image distortion during up-sampling and down-sampling. The decomposition transform process is shown in the following Figure 1.

B. DUAL CHANNEL PULSE COUPLED NEURAL NETWORK

DC-PCNN, similar to PCNN, is a single-layer feedback-type network model proposed based on the principle of cat vision, which can effectively extract image information without learning and training, and it is a strongly adaptive system. It has multiple neurons, each of which contains three parts: the received input domain, the connection modulation domain, and the pulse generation domain, respectively. The structure of the DC-PCNN model is shown in the following Figure 2, and its mathematical expression is as follows:

$$FA_{ij}(n) = SA_{ij} \tag{1}$$

$$FB_{ij}(n) = SB_{ij} \tag{2}$$

$$UA_{ij}(n) = FA_{ij} * \left(1 + \beta_A V_L \sum_{pq} \mathbf{W}_{pq} Y_{pq}(n-1)\right) \tag{3}$$

$$UB_{ij}(n) = FB_{ij} * \left(1 + \beta_B V_L \sum_{pq} \mathbf{W}_{pq} Y_{pq}(n-1)\right) \tag{4}$$

$$U_{ij}(n) = e^{-\alpha_u} U_{ij}(n-1) + \max\{FA_{ij}(n), FB_{ij}(n)\} \tag{5}$$

$$Y_{ij}(n) = \begin{cases} 1, & if\ U_{ij}(n) > \theta_{ij}(n-1) \\ 0, & otherwise \end{cases} \tag{6}$$

$$\theta_{ij}(n) = e^{-\alpha_\theta} \theta_{ij}(n-1) + V_\theta Y_{ij}(n) \tag{7}$$

In the above expressions: n is the number of iterations, SA_{ij}, SB_{ij} are the two external input excitation, FA_{ij}, FB_{ij} is the neural feedback input, β_A, β_B is the link strength coefficient, V_L, V_θ is the link amplification coefficient and the threshold amplification coefficient, respectively, $\mathbf{W}_{pq}$ is the synaptic link power coefficient matrix, Y_{ij} is the binary output result of this neuronal pulse, Y_{pq} is the binary output of neuron impulses in the previous iteration, and the link strength of this iteration is determined by the previous impulse output, UA_{ij}, UB_{ij}, U_{ij} is the neuronal internal activity term, α_u, α_θ is the internal activity term decay coefficient and the threshold decay coefficient, respectively, and θ_{ij} is the dynamic threshold.

Eq. 6 shows that when comparing U_{ij} with θ_{ij} the ignition, the output of the completed neuron, whose value is 0 or 1, so the PCNN produces a binary image after each iteration, and then θ_{ij} will decay exponentially according to Eq. 7 to reach the next ignition degree, and U_{ij} is continuously adjusted by a link strength and β. When PCNN performs image fusion, PCNN is a two-dimensional single-layer laterally connected neural network, and each image pixel is connected as a neuron. Meanwhile, the link strength parameters, amplification coefficient, attenuation coefficient, link weight matrix, etc. are set by empirical values, which will have some influence

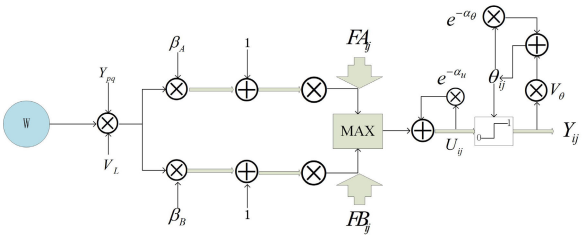

FIGURE 2. The architecture of the DC-PCNN network.

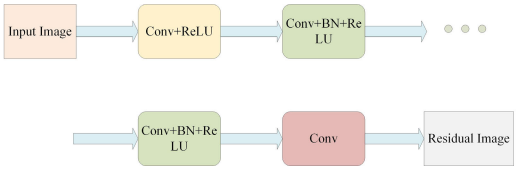

FIGURE 3. The architecture of the DnCNN network.

on the image fusion effect, and the adaptive modification of some of these parameters will be explained later to improve the fusion effect and avoid the artificial influence of empirical factors.

C. DENOISING CONVOLUTIONAL NEURAL NETWORK

DnCNN is a convolutional neural network built on the basis of VGG, and its network structure mainly consists of three parts, the first part is Conv+ReLU, the second part is several layers of Conv+BN+ReLU, the third part is Conv, the number of network layers is 17 or 20 layers. Inside the model does not perform long jump connections like ResNet, but by learning predictions for image noise and reducing to noise-free images by subtracting noisy images from the input images after residual learning, the network model is shown in Figure 3. In the training process of the DnCNN network model, the mean square error (MSE) between the real residual image and the network output is used as the loss function to back propagate to correct the network parameters.

$$L(\theta) = \frac{1}{2N} \| R(\mathbf{y}_i; \theta) - (\mathbf{y}_i - \mathbf{x}_i) \|^2 \tag{8}$$

In Eq. 8, $L(\theta)$ denotes the learning of the network parameter θ, N is the number of samples, $R(\mathbf{y}_i; \theta)$ is the network residual output, $\mathbf{y}_i$ is the noisy image, and $\mathbf{x}_i$ is the noise-free image.

D. FAST AND FLEXIBLE DENOISING CONVOLUTIONAL NEURAL NETWORK

The FFDNet model is an optimization improvement based on the DnCNN model, which has a higher requirement for noise and requires uniformly distributed Gaussian noise, but is also able to suppress a certain range of noise. Real noise is inter-signal dependent and correlated across color channels, and is not uniformly distributed Gaussian noise, so the input to FFDNet is an estimated noise map, which can effectively maintain image details and suppress noise,

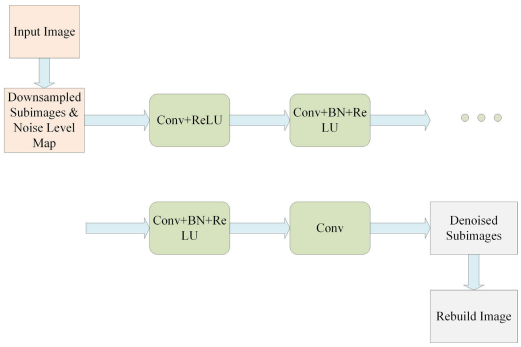

FIGURE 4. The architecture of the FFDNet network.

and can handle higher complexity levels of noise and spatial variation noise. Because optical remote sensing images have very complex texture details, the noise reduction capability of FFDNet is outstanding in the case of high-level noise, which can also be verified in the subsequent experiments in this paper.

Besides, the network input of FFDNet is multiple subgraphs generated by down-sampling the input image, and the final output is up-sampled through the subgraphs. This is similar to part of the principle of this paper, which also processes the subgraphs after sampling, but NSCT uses non-down-sampling filtering decomposition when transforming the decomposed images, which can avoid the image distortion caused by up-sampling and down-sampling to some extent. The purpose of this design of FFDNet is to increase the perceptual field while down-sampling to obtain the appropriate network depth. The FFDNet is designed with 15 layers and the convolution of 3×3 will obtain the perceptual field of 62×62, while the CNN with 15 layers will only obtain the perceptual field of 31×31, which also makes the FFDNet has better noise reduction ability in the case of the high level of complex noise. The orthogonal matrix is also used to initialize the network parameters and improve the efficiency of network learning and training. The structure of the FFDNet network model is shown in the following Figure 4:

The purpose of using residual learning is that when the residual is 0, the mapping between the stacking layers is constant and easier to optimize, and at the same time, when the image noise level is small, the residual between the noisy image and the noiseless image is very small, so the original authors introduced residual learning [30] into the image noise reduction. The DnCNN model also has the advantage of introducing Batch Normalization (BN) [31], in the process of deepening with the depth of the network, its distribution will gradually shift or change, which will cause the gradient of the underlying neural network to disappear during back propagation, while BN will normalize the network neuron input values to a standard normal distribution with a mean of 0 and a variance of 1 to avoid gradient disappearance, accelerate the learning convergence efficiency, and improve the training speed.

E. GUIDED FILTER

The key point in the guided filter is the local linear model. When a point on a function is linearly related to the adjacent partial points, then multiple consecutive local linear models can be used to form a complex function model, so that when the value of a point on the model is needed, only the mean value of the linear model at that point needs to be calculated.

Therefore, the guided filter starts from a linear model, where the guided image has a linear connection with the input image. And the input image is guided with the guided image as the reference information image. Finally, the filtered image is output by the mean filtering calculation model. When filtering the image, the current pixel is set to have a linear relationship with the neighboring pixels, and the guidance formula is:

$$\mathbf{q}_i = a_k \mathbf{I}_i + b_k, \forall i \in \omega_k \tag{9}$$

In Eq. 9, $\mathbf{q}_i$ is the guided image $\mathbf{I}_i$ centered on the pixel i, the linear transform filtered image of the window ω_k with radius k, a_k and b_k are the coefficients to be determined.

The guided filter has the edge-preserving property of bilateral filtering [32] and the avoidance of gradient inversion [33] artifacts, which can effectively enhance the image details, so it is introduced into the texture detail stimulation of sub-bands under the NSCT domain in this paper.

III. PROPOSED METHOD

A. FRAMEWORK PROCESS

The framework of this paper is divided into the following 4 parts, and its flow chart is shown Figure 5.

Step1. Mixed noise preprocessing. Firstly, the image pixel points are discriminated by IMFLED, and the pixel points are divided into signal points and noise points, which are removed iteratively after detection by local extreme noise. Then, the images with only Gaussian noise are removed by DnCNN and FFDNet respectively. After preprocessing, the low-noise images DnCNN Image and FFDNet Image are obtained for fusion reconstruction.

Step2. NSCT decomposition transforms the input image. Firstly, the DnCNN Image is decomposed directly to obtain the corresponding low-frequency sub-bands Lowpass Subband-A and high-frequency sub-bands Highpass Subband-A, while the noise-reduced images of DnCNN and FFDNet, respectively, are used as the inputs of the two channels of Dual-PCNN for fusion pre-processing to obtain cleaner images Pretreatment Image, and then the fused images are decomposed to obtain the corresponding low-high-frequency sub-bands Lowpass Subband-B, Highpass Subband-B.

Step3. The low and high-frequency sub-bands are filtered by the guided filter for detail stimulation. The GF-Lowpass Subband-A is obtained by filtering the Lowpass Subband-A by guiding its own image, and for DnCNN high-frequency sub-bands, the DnCNN noise-reduced guided filtered detail layer GF-DnCNN Image-Detail layer is obtained first, which is enhanced by beta parameter and then fused to the high-frequency sub-bands to obtain the DnCNN high-frequency sub-bands Enhance-Highpass Subband-A with enhanced edge contours and detail information. The same enhancement is applied to the fused image sub-bands to obtain sub-bands with higher energy coefficients.

Step4. NSCT reconstructed images. Firstly, the two enhanced low-frequency sub-bands GF-Lowpass Subband-A, GF-Lowpass Subband-B are imported into the two channels of Dual-PCNN to obtain the low-frequency sub-bands Fuse-Lowpass Subband with richer texture details after fusion, and then the high-frequency sub-bands Fuse-Highpass Subband are fused in the same way to obtain the high-frequency sub-bands with clearer contour structure and richer energy information. Finally, the sub-bands are reconstructed by NSCT to obtain the final image.

B. IMAGE PREPROCESSING

1) IMPULSE NOISE PREPROCESSING

In this article, a mixture of impulse noise and Gaussian noise is chosen to simulate the complex situation of image noise reduction and reconstruction. In image noise reduction, the purpose of mixing multiple noise types is to simulate the situation that multiple noise types may exist in the actual image. Impulse noise and Gaussian noise are the most common types of noise in the real world and also in remote sensing images, so impulse noise and Gaussian noise are chosen to be mixed for simulation. And usually image denoising algorithms usually choose Gaussian noise for simulation, because it is closer to the unknown real noise. In summary, this paper chooses a mixture of impulse noise and Gaussian noise for the algorithm study. After the experimental validation, it is found that IMFLED combined with DnCNN and FFDNet can obtain excellent denoising results. In the low-noise case, DnCNN can achieve better performance due to its excellent modeling ability, and in the high-noise case, FFDNet has a larger perceptual field and is more capable of removing strong noise. In this case, the relevant parameters in IMFLED are set according to the original literature.

Compared to the classic impulse noise removal method, IMFLED is divided into noise detection and noise filtering, first by setting a noise detection window, and then operating with a pixel point as the center, if the maximum or minimum value in the window for this pixel point itself, it is a noise point, and vice versa is a signal point, noise detection will finally generate a binary image that represents the image noise. Noise filtering is the transformation of noise points in the window into signal points by multiple iterations. The connection domain property of PCNN will make the other neurons in its domain with approximate input excitation when the neuron is ignited to activate the output pulse in the next iteration, that is, the point is an impulse noise point, so PCNN has an excellent ability for impulse noise removal. It has been introduced into the field of image noise reduction. Also to prove the sensitive property of PCNN for noise, it is therefore selected as one of the comparison methods for

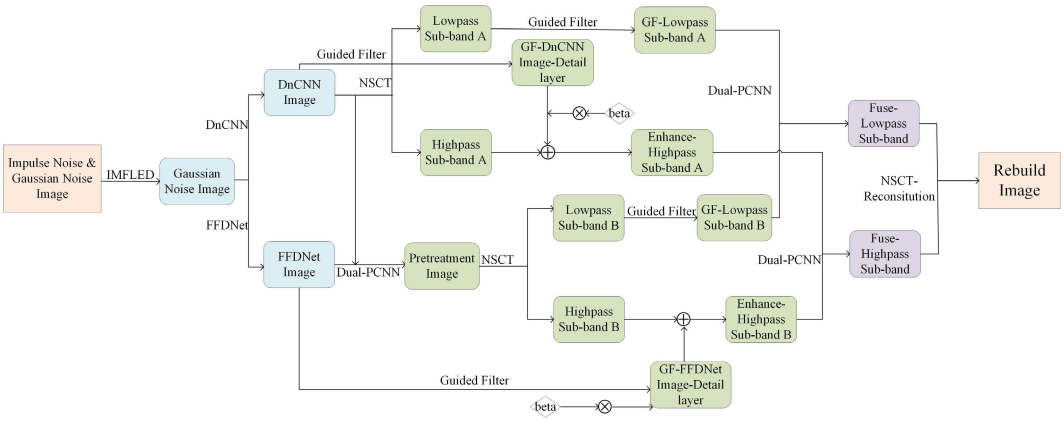

FIGURE 5. The architecture of the proposed model.

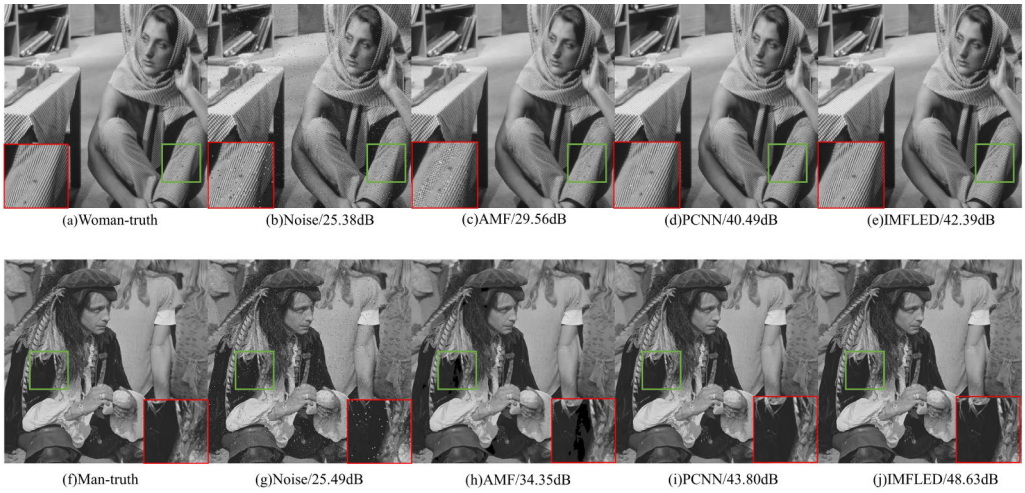

FIGURE 6. Denoising results of the Woman and Man image from Set12 with the pulse noise density 0.01.

impulse noise removal methods. PCNN is a neural network that can extract image features without training, and the setting of its network parameters is extremely important. In this article, we set the connection neuron weights $\begin{bmatrix} 0.5 & 1 & 0.5 \\ 1 & 0 & 1 \\ 0.5 & 1 & 0.5 \end{bmatrix}$, connection strength 0.09, decay time constant 0.1, dynamic threshold 323. Finally, in order to verify the pulse removal capability of IMFLED, this paper will be compared with the classical adaptive median filtering and PCNN algorithms to verify the quantitative evaluation by the Peak Signal-to-Noise Ratio (PSNR) and Structural Similarity ratio (SSIM) [34]. Adaptive median filter (AMF), which introduces adaptivity based on the conventional median filter, is a very classical nonlinear filter for removing impulse noise, so it is selected as one of the comparison methods for impulse noise removal methods. The experimental impulse noise densities are 0.001, 0.005, 0.01, and 0.05, where the impulse noise density indicates the proportion of noisy pixels, that is, the proportion of pixels affected by noise in the image. An impulse noise density of 0.001 means that only 1 out of 1000 pixels is affected by impulse noise, 0.005 means that 5 out of 1000 pixels are affected by impulse noise, 0.01 means that 10 out of 1000 pixels are affected by impulse noise, and 0.05 means that 50 out of 1000 pixels are affected by impulse noise.

From the bolded black font data in Table 1 and Table 2, we can find that IMFLED has the most stable and best performance for different degrees of impulse noise removal, and its PSNR value and SSIM value are the highest. It is also found that PCNN has a good effect on the removal of impulse noise, which indicates to a certain extent that PCNN has a certain effect on the recognition and extraction of image features. Overall, IMFLED has a greater enhancement effect compared to PCNN and AMF for impulse noise preprocessing. In Figure 6, the image in the red box is the enlarged image of the green box image, which is convenient for comparative observation and can verify the conclusions obtained in the table. In the Woman image, it can be found that the detailed structure in Figure 6(e) is most similar to Figure 6(a), and some noise remains in Figure 6 (c) and Figure 6(d). In the

TABLE 1. The woman experimental results: the evaluation index of PSNR (dB)/SSIM.

Method	0.001	0.005	0.01	0.05
AMF	29.63/0.9396	29.63/0.9398	29.56/0.9395	29.27/0.9378
PCNN	52.44/0.9997	43.76/0.9975	40.49/0.9956	33.05/0.9779
IMFLED	**53.53/0.9998**	**45.71/0.9988**	**42.39/0.9975**	**35.63/0.9876**

TABLE 2. The man experimental results: the evaluation index of PSNR (dB)/SSIM.

Method	0.001	0.005	0.01	0.05
AMF	34.12/0.9492	34.13/0.9493	34.35/0.9504	35.64/0.9564
PCNN	54.13/0.9996	47.88/0.9987	43.80/0.9967	35.25/0.9819
IMFLED	**59.87/0.9998**	**51.37/0.9992**	**48.63/0.9984**	**41.01/0.9911**

Man image, it can be found that Figure 6(h) has the worst effect, and it cannot effectively judge the pixel points close to or extreme values of the original image, resulting in large black spots remaining in the image, while Figure 6(j) can effectively distinguish the noise points from the signal points by multiple iterations, and after detecting the noise, it can remove the noise while retaining the complete texture details to avoid blurring the image.

2) GAUSSIAN NOISE PREPROCESSING

Gaussian noise removal is mainly divided into several types of spatial domain filtering [35], transform domain filtering [36], denoising based on Partial Differential Equation (PDE) [37], denoising based on non-local self-similarity [38], and denoising based on deep learning [39]. They have their own characteristics, such as PDE can retain the image edge structure information better, but the step effect will occur, and the diffusion equation method will show an overfitting phenomenon, while the denoising effect decreases significantly with the increase of noise level. Non-local self-similarity-based denoising such as the BM3D algorithm, which is one of the current standards of denoising algorithms, can effectively preserve similar texture information of images globally. At present, deep learning performs very well in the field of image denoising, such as DnCNN and FFDNet optimized on this basis can achieve more excellent results compared with PDE and BM3D, which are fully verified by experiments in the original literature of them.

There are some differences between them. DnCNN benefits from its excellent modeling ability and has better noise reduction ability in the low-noise case, but as the noise intensity increases, the noise reduction ability of FFDNet performs more outstandingly because its perceptual field is larger compared with other CNNs and its ability to acquire image features is stronger. The network structures and related parameters of DnCNN and FFDNet are set according to the original literature.

Therefore, they are used for Gaussian noise reduction of the image after IMFLED processing respectively in this article, and then fusion preprocessing is performed to obtain preprocessed images with better image clarity, texture details, and structural contours for reconstruction.

C. SIMPLIFIED PARAMETRIC ADAPTIVE DUAL-CHANNEL PCNN MODEL

PCNN and DC-PCNN require the artificial empirical setting of multiple parameter values, which affects the fusion effect to some extent, while simplified adaptive Dual-PCNN is a direct matrix operation on the matrix of pixel points in the two images in the dual channel, which can be adaptively obtained for the relevant part of parameters.

The link input of DC-PCNN in Eq. 3 and Eq. 4 are determined by the synaptic link power coefficient matrix $\mathbf{W}_{pq}$ and the link amplification coefficient V_L. Firstly, the pulse output matrix $\mathbf{Y}$ is set as the matrix **zeros**, and then the link input matrix is set as the matrix **ones** if the sum of the elements $\mathbf{Y}$ in the iterative loop is less than or equal to 0, and vice versa set as the matrix **zeros**. The adaptive link intensity coefficient β'_A is obtained by convolving the image pixel matrix of channel A with the Laplace operator in two dimensions, and the adaptive link intensity coefficient β'_B is obtained for the same reason. At the same time, the decay term of the internal activity term U_{ij} of the neuron in Eq. 5 is simplified, and the empirical setting of the internal activity term decay coefficient is avoided to speed up the operation efficiency. The modifications of Eq. 3, Eq. 4, and Eq. 5 are as follows:

The Laplace operator template is $\begin{bmatrix} -1 & -1 & -1 \\ -1 & 8 & -1 \\ -1 & -1 & -1 \end{bmatrix}$.

$$\mathbf{L} = \begin{cases} \mathbf{ones}, & if \sum\sum Y_{pq} \le 0 \\ \mathbf{zeros}, & otherwise \end{cases} \tag{10}$$

$$\mathbf{UA}(n) = \mathbf{FA} * \left(\mathbf{con} + \beta'_A \mathbf{L}\right) \tag{11}$$

$$\mathbf{UB}(n) = \mathbf{FB} * \left(\mathbf{con} + \beta'_B \mathbf{L}\right) \tag{12}$$

$$\mathbf{U}(n) = \max\{\mathbf{FA}(n), \mathbf{FB}(n)\} \tag{13}$$

FIGURE 7. Decomposing results of the Castle image from BSD68.

Eq. 10, **L** is the link input, Eq. 11 and Eq. 12 are the matrix with all 1. After obtaining the pulse ignition matrix **U**, the ignition pixel points are determined by comparing **UA** with **UB**, and then assembled into the new pixel matrix to obtain the final fused image **Fuse**. The Eq. 14 is as follows:

$$\mathbf{Fuse}_{ij}=\begin{cases}\mathbf{SA}_{ij},\ if\ \mathbf{UA}_{ij}=\mathbf{U}_{ij}\\ \mathbf{SB}_{ij},\ if\ \mathbf{UB}_{ij}=\mathbf{U}_{ij}\end{cases} \tag{14}$$

D. LOW AND HIGH FREQUENCY SUB-BAND FUSION RULES

1) IMAGE DECOMPOSITION

In this experiment, the image decomposition is performed by NSCT pair with a decomposition level of [0,1].Firstly, the original image is divided into 1 low-frequency sub-band and 1 high-frequency sub-band, and this high-frequency sub-band is decomposed in one direction. Then the low-frequency sub-band is decomposed, and the high-frequency sub-band is decomposed in two directions for the 2nd time. Finally, a total of 1 low-frequency sub-band and 3 high-frequency sub-bands are generated. The pyramid filter is chosen as maxflat and the direction filter is chosen as dmaxflat7, with the decomposition level of D= [0,1]. The image with impulse noise of 0.001 and Gaussian noise level of 10 is noise reduced by using IMFLED and DnCNN through the framework of this paper, and then decomposed by NSCT as shown in Figure 7.

For easy observation, Figure 7(d), (e), and (f) are shown enhanced, as shown in Figure 8:

Figure 7(c) shows that the low-frequency sub-band mainly retains most of the image information, Figure 7(d) indicates all the high-frequency contour structure information in one direction for the high-frequency sub-band, and Figure 7(e) and (f) indicate the high-frequency information in two directions after decomposing the high-frequency sub-band from the second time. It can be found that NSCT can effectively separate the low-high frequency image information, and at the same time, the high-frequency image possesses the complete contour edge structure within, which provides effective help for the subsequent image edge structure enhancement in this article.

2) SUB-BANDS ENHANCEMENT

This experiment is to enhance the image edge texture details by guided filtering. Since the guide filter requires the guide image and the input image to be set as the same image if the edge-preserving effect is to exist, and also the processing window radius and the adjustment parameter have a relatively large impact on the filtering effect, the optimal parameters should be selected according to the requirements [40]. After several experiments, the radius was set to 4 and the adjustment parameter to 0.2 based on the combined effect.

The output of the guided filter is the linearly transformed image of the input image with the reference information of the guided image, which has an excellent smoothing effect and edge preservation ability. The base layer image **q** is obtained by Eq. 9, and then the detail layer image **d** is obtained by operation with the input image **p**, as shown in Eq. 15:

$$\mathbf{d}=\mathbf{p}-\mathbf{q} \tag{15}$$

Figure 9(a) is the base layer image after smoothing by guided filtering, which effectively preserves the texture information of the image, so Figure 7(c) will be guided filtered to enhance the detailed texture representation. The edge contour information has higher structural similarity between Figure 7(d) and Figure 9(b), and Figure 9(b) retains more complete texture details, so this paper will enhance and improve the high-frequency contour and texture information in Figure 7(d) by Figure 9(b).

$$\mathbf{E}=\mathbf{q}+\beta_d\mathbf{d} \tag{16}$$

Eq. 16, **E** denotes the enhanced image and β_d denotes the enhancement factor. Figure 9(d) is the display of Figure 9(b) after enhancement by coefficients, and it can be found that for the image edge contour information, structural information is highlighted to a greater extent, but there is a halo phenomenon [41], produced by the bootstrap filtering. Figure 9(c) is the display of the original image after enhancement, its image brightness is enhanced and energy information is abundant.

Figure 10(a) is all the pixel values of Figure 7(d) in 156 columns, while Figure 10(b) is all the pixel values

(a)Enhance-High-frequency subband-B | (b) Enhance-High-frequency subband-C | (c) Enhance-High-frequency subband-D

FIGURE 8. Enhancing high frequency sub-bands.

(a) Basic layer | (b) Detail layer | (c)Enhance Image | (d)Enhance detail layer

FIGURE 9. Filtering and Enhancing results of the Castle image from BSD68.

of Figure 9(d) in 156 columns are shown, and it can be found that there are many similarities in the extreme part of Figure 10(a) and 10(b), while the peak fluctuation of Figure 10(b) is larger, which indicates that it is more sensitive to the change of pixel gradient, reflecting the characteristics of guided filtering, and the information retained in the detail layer is more perfect, which can effectively enhance the high-frequency sub-bands. Figure 10(c) is the enhanced high-frequency sub-band after the NSCT decomposition.

3) SUB-BANDS FUSION RULES

The low-frequency sub-band contains most of the image energy and some of the texture details, while the image energy can determine the spatial relationship of the fused image and the texture details can determine the clarity of the image. The high-frequency sub-band contains the high-frequency contour information of the image and reflects the edge structure of the image. In this paper, the image is reconstructed by enhancing the fusion sub-bands in the following 4 steps:

Step1. The image after DnCNN preprocessing is set as $\mathbf{I}_A$, and the image after DnCNN and FFDNet fusion is set as $\mathbf{I}_B$. After the image $\mathbf{I}_A$ is decomposed by NSCT, the low-frequency sub-band $\mathbf{L}_{a1}$ is generated, and the high-frequency sub-bands $\mathbf{H}_{a2}$, $\mathbf{H}_{a3}$, $\mathbf{H}_{a4}$ are generated. After the image $\mathbf{I}_B$ is decomposed by NSCT, the low-frequency sub-band $\mathbf{L}_{b1}$ is generated, and the high-frequency sub-bands are $\mathbf{H}_{b2}$, $\mathbf{H}_{b3}$, $\mathbf{H}_{b4}$ are generated.

Step2. The low-frequency sub-band $\mathbf{L}'_{a1}$ is obtained by guided filtering as the guiding and input image $\mathbf{L}_{a1}$, and the detail layer image is obtained by guided filtering as the guiding and input image $\mathbf{I}_A$, and then fused with $\mathbf{H}_{a2}$ after enhancement by the method in section III-D2. After that, we can obtain the enhanced high-frequency sub-band $\mathbf{H}'_{a2}$. Similarly, the enhanced low-frequency sub-band $\mathbf{L}'_{b1}$ can be obtained as $\mathbf{L}_{b1}$, and the enhanced high-frequency sub-band $\mathbf{H}'_{b2}$ is obtained by $\mathbf{I}_B$, $\mathbf{H}_{b2}$.

Step3. The final low-frequency sub-band $\mathbf{L}_{s1}$ is obtained by fusing $\mathbf{L}'_{a1}$ with $\mathbf{L}'_{b1}$ the simplified adaptive Dual-PCNN fusion model, the high-frequency sub-band $\mathbf{H}_{s2}$ is obtained by fusing $\mathbf{H}'_{a2}$ with $\mathbf{H}'_{b2}$, the high-frequency sub-band $\mathbf{H}_{s3}$ is obtained by fusing $\mathbf{H}_{a3}$ with $\mathbf{H}_{b3}$, the high-frequency sub-band $\mathbf{H}_{s4}$ is obtained by fusing $\mathbf{H}_{a4}$ with $\mathbf{H}_{b4}$.

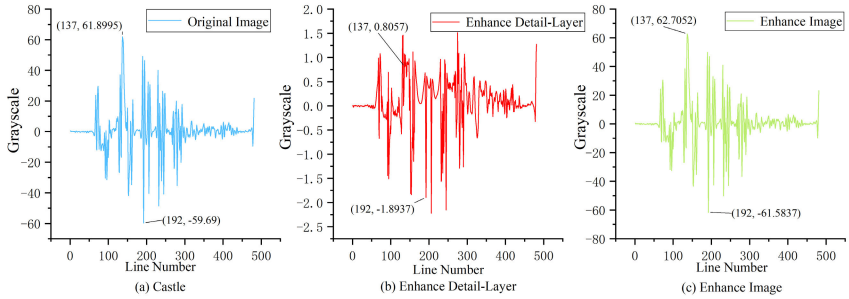

FIGURE 10. Grayscale values of the Castle image column 156 from BSD68.

Step4. $\mathbf{L}_{s1}$, $\mathbf{H}_{s2}$, $\mathbf{H}_{s3}$ and $\mathbf{H}_{s4}$ are reconstructed by NSCT with inverse conversion to obtain the reconstructed fused images.

IV. EXPERIMENTAL RESULTS AND ANALYSIS

To verify the performance effectiveness of the framework method in this article, six sets of grayscale images from BSD68 were selected for the experiments, as well as a one-view single-band image of the Landsat 8 satellite in Guilin City, Guangxi Province, China. Grayscale images are generalized as source images for simulation experiments. Grayscale image processing can be involved in fields such as computer vision and medical image processing, which facilitates universal communication between multiple fields. When the simulation experiments are completed using grayscale images, they can be applied to other fields, such as remote sensing image processing in this paper. Meanwhile, the information on grayscale images is more focused on image brightness, contrast, and texture, which is more suitable for the verification of algorithm models and is less computationally intensive and more efficient. Therefore, after completing the simulation experiments using grayscale images, the method model is applied to the experiments of optical remote sensing images.

Remote sensing images are wide-area, comprehensive, and multifaceted, and can use multiple waveband data in a wide range to obtain feature information from different angles and dimensions, including the spatial distribution, types, and characteristics of features. Meanwhile, optical remote sensing images have strong research value from the perspective of image processing with complex texture information and spatial energy information. Meanwhile, the reason for choosing impulse noise and Gaussian noise for hybrid modeling is that these two types of noise are common noise types in remote sensing images, which can have a large impact on the visual quality and quantitative analysis of remote sensing images, as well as cause local discontinuities in the images and interfere with the segmentation and classification of images. Therefore, removing the noise can make the image clearer and enable a series of operations such as feature identification, feature extraction, and feature classification to be performed accurately.

The quantitative indexes were evaluated by the Peak Signal-to-Noise Ratio (PSNR), Structural Similarity (SSIM), and Edge Preservation Index (EPI) [42], which reflect the difference between the reconstructed image and the ideal reference image, and the Average Gradient (AG) [43], Spatial Frequency (SF) [44], and information Entropy (EN) [45], which measure the good or bad image quality based on the statistical feature values of the reconstructed image itself, where the larger the value of AG, SF, EN, and PSNR the better the effect, and the closer the value of SSIM and EPI to 1 the better the effect. The experiments in this study were run in Matlab (R2020a) environment with 13th Gen Intel(R) Core (TM) i9-13900HX 2.20 GHz and 16 GB RAM.

A. GRAYSCALE IMAGE EXPERIMENT

The experimental data set is 6 grayscale images with a pixel size of 321×481 in BSDS [46], impulse noise with the density of 0.001 and Gaussian noise with the noise level of 10, 15, and 20 are added to each image respectively, and a total of 18 noisy images have experimented.

Gaussian noise levels of 10, 15, and 20 are the standard deviations of Gaussian noise. The standard deviation indicates the degree of dispersion of a random variable or data set, and its larger value indicates a wider scattering of the data and a greater intensity of the noise. The Gaussian noise used in this study is incremented by 5 units on a scale of 0-255, and then the different levels of Gaussian noise are normalized to between 0 and 1 to facilitate computation and improve the performance of the algorithm.

At the same time, the reason for choosing the 0.001 value of pulse noise density for the experiment is that from Table 1 and Table 2, it can be found that the effect of IMFLED is the best at different pulse noise densities, and the purpose of choosing 0.001 pulse noise density for the experiment in this paper is to ensure that the framework proposed in this paper is useful for mixed noise removal while minimizing the interference with the original image information. Although IMFLED can effectively identify noise points, its principle of replacing noise points based on neighboring pixels still interferes with the original image information. Meanwhile, under normal circumstances, the impulse noise density of remote sensing images will not be at a very

FIGURE 11. The 6 widely used testing images from BSD68.

high density, so a noise density of 0.001 is chosen for the experiment.

The method in this article is compared with BM3D, DnCNN, FFDNet, BM3D-DnCNN-Dual-PCNN, BM3D-FFDNet-Dual-PCNN, and DnCNN-FFDNet-Dual-PCNN for experiments to evaluate qualitative and quantitative aspects.

Figure 12 shows the image fusion reconstruction results of the above seven algorithm models, from top to bottom row 1 is six mixed noise images with impulse noise density 0.001 and Gaussian noise level 20, from row 2 to row 8 are BM3D, DnCNN, FFDNet, BM3D-DnCNN-Dual-PCNN, BM3D-FFDNet-Dual-PCNN, DnCNN-FFDNet-Dual-PCNN and the noise reduction fusion reconstructed images of the method in this paper. BM3D-DnCNN-Dual-PCNN, BM3D-FFDNet-Dual-PCNN, and DnCNN-FFDNet-Dual-PCNN are to retain the denoising processing part in the framework of this paper, and then directly fuse the denoised images from different denoising methods by the Dual-PCNN method proposed in this paper for multi-source image fusion, but which does It does not include the sub-band fusion enhancement part in the NSCT domain.

From the images, it can be found that the worst BM3D effect can be clearly observed in the red box region, where there is blurring of the image and loss of image texture details. This is because BM3D is an algorithm based on non-local similarity theory, which possesses good results for images with high structural repetition but performs poorly in the case of complex textures.

The images in the third and fourth rows are the reconstructed images with noise reduction from the DnCNN and FFDNet network models, respectively. In the red area of Oldman, it is found that FFDNet retains more texture detail in the middle of the forehead and wrinkles, and has higher contrast, making the portrait more three-dimensional; in the red area of Antelope, it is found that the overall brightness of FFDNet is lower, closer to the original image, and the overall visual effect is better.

The fifth and sixth rows show the images after BM3D is fused with DnCNN and FFDNet through Dual-PCNN, respectively, because the image quality acquired by BM3D is poor, so although good results are obtained in some areas with high structural similarity, such as the window area of the Building image, the overall reconstruction effect of the image is pulled down, such as in the Mushroom image In the red box, the longitudinal fold texture information of the mushroom surface is severely lost.

In the seventh row, DnCNN and FFDNet are fused with Dual-PCNN to reconstruct the images, and the red box areas from Oldman, Mushroom, Pottery, and Antelope images, especially the horizontal and vertical striped areas, have clearer contours and are more consistent with the visual observation. Our conclusion can be verified from Figure 13 which shows that Dual-PCNN is effective for image reconstruction.

The deep learning-based network model and the associated fusion model can extract image features well by modeling and expanding the perceptual field [47], which can effectively preserve the detailed textures of the image. Therefore, from the experimental results, the DnCNN-FFDNet-Dual-PCNN fused image quality by Dual-PCNN has some improvement compared with the original DnCNN and FFDNet images, which indicates the effectiveness of Dual-PCNN in fusing reconstructed images. Also separating the sub-band fusion module in the NSCT domain illustrates the excellent performance of the sub-band fusion rules and bootstrap filtering proposed in this paper.

The proposed method in this paper can be seen in the red-boxed area to retain the details well, and at the same time can show the contour information of the image well such as the stripes in the red box of Pottery in Figure 12(e) is more prominent, thanks to the enhancement of the high-frequency sub-bands. The texture information on the forehead surface of the portrait in the red frame area of Oldman is more fully preserved compared with methods such as DnCNN-FFDNet-Dual-PCNN, and the contrast between the rocks in the red frame area of Antelope is stronger, and the difference between them can be clearly observed, and the rock reconstruction effect is more three-dimensional. In addition, after the image fusion by Dual-PCNN, the energy information is well preserved and the visual effect is better.

In Figure 13, the blackened data indicate the optimal data. The method in this paper is always optimal in PSNR and EPI, and PSNR is only lower than FFDNet in Pottery and is also optimal or suboptimal in SSIM. The most obvious reason for the difference between EPI and other algorithms' EPI values is that this paper is based on NSCT and optimizes its fusion

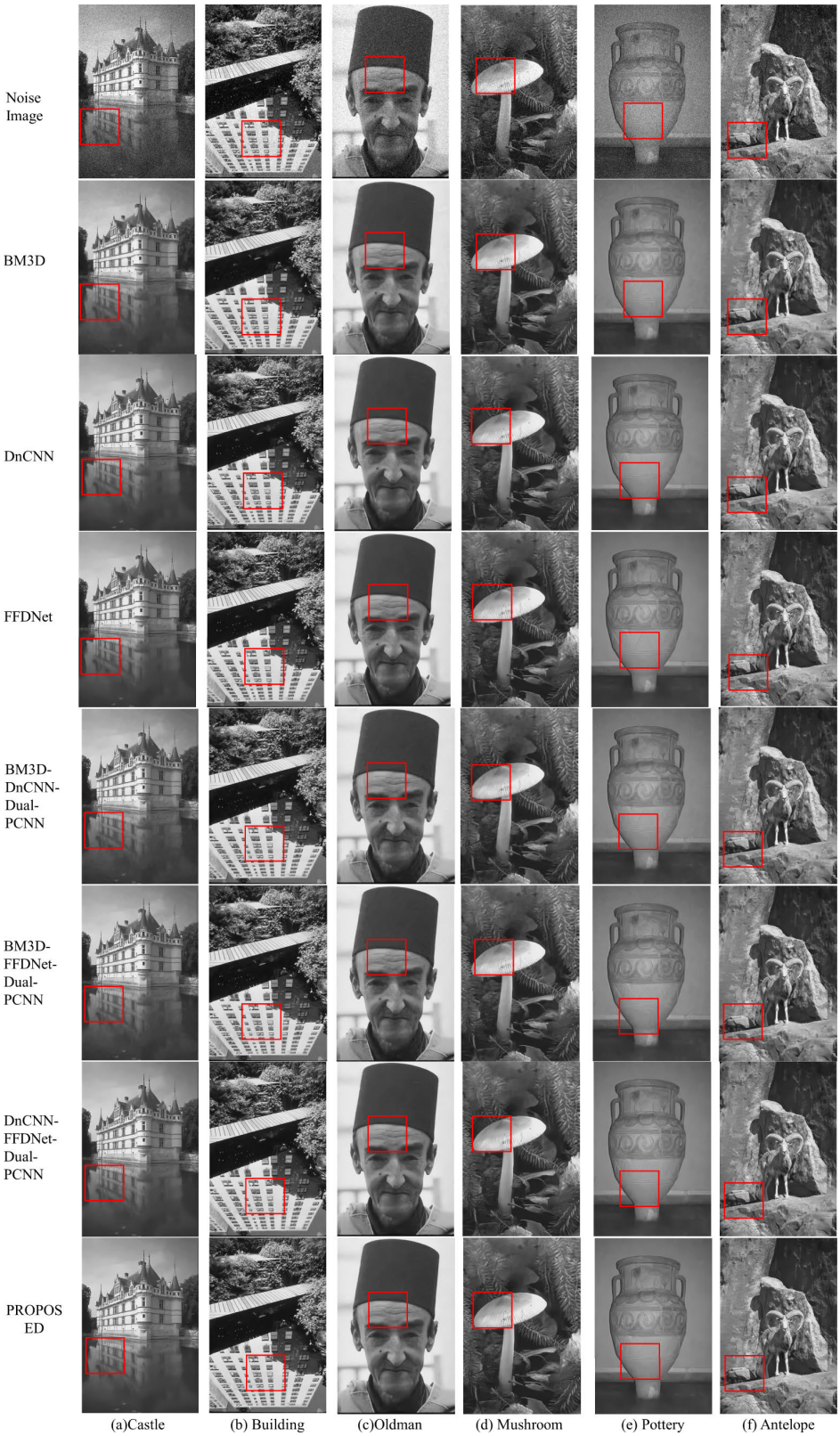

FIGURE 12. Grayscale image rebuilding results by different methods on Mixed noise.

rules for low-frequency sub-bands and high-frequency sub-bands, which can effectively preserve the edge and detail information of the image. At the same time, this paper also introduces guided filtering to preserve the image edge detail

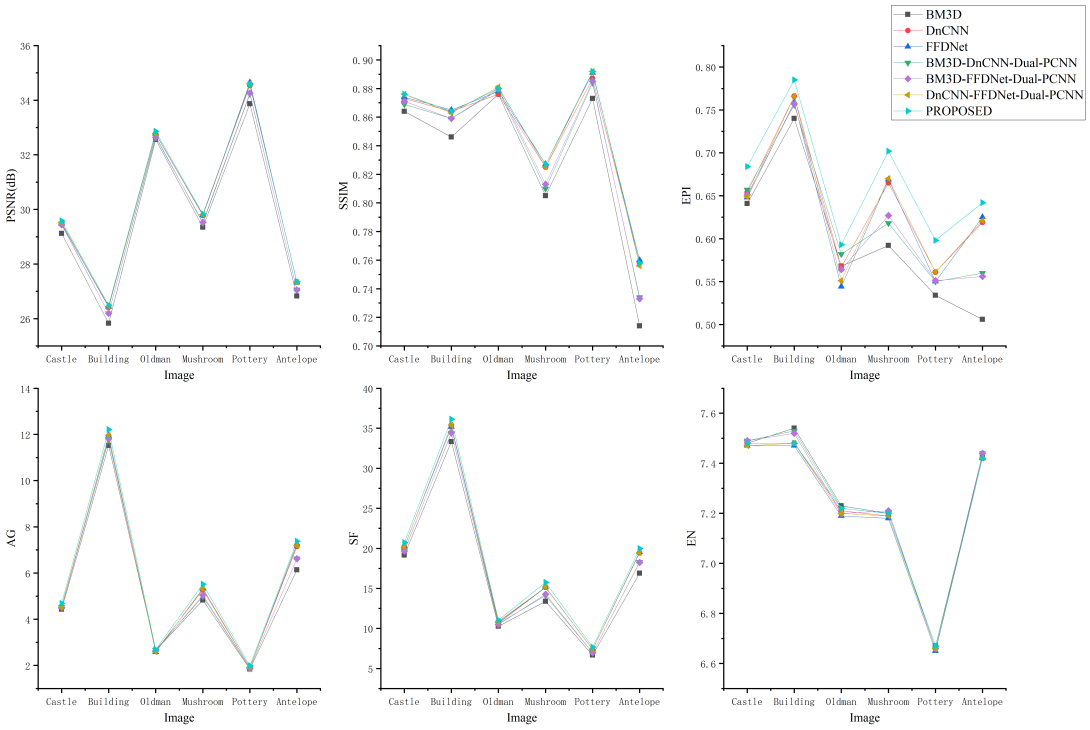

FIGURE 13. Quantitative evaluation index for grayscale image reconstruction.

information and prevent it from being lost in the decomposition process. By fusing the detail layer with the sub-bands, the edge contour information of the image can be highlighted more effectively. The edge contour structure has outstanding performance.

In Figure 13, the method of this paper has also been in the best performance in AG and SF, and the reconstructed image retains rich image energy information and high-frequency information, while it is also in an optimal or sub-optimal situation in EN, which comprehensively can strongly indicate that the method of this paper achieves better results in image fusion quality.

Overall, through six quantitative evaluation indexes and visual subjective experience [48], the method in this paper performs image noise reduction processing under the interference of multiple complex noise situations, and then fuses and reconstructs the multi-source images to obtain outstanding results, which illustrates the effectiveness of the method in this paper.

B. REMOTE SENSING IMAGE RECONSTRUCTION EXPERIMENT

A Landsat 8 satellite single-band orthophoto of a view in Guilin City, Guangxi Province, China, in September 2018 was cropped to a pixel size of 784×760 for experiments. And impulse noise with a density of 0.001 and Gaussian noise with noise levels of 10, 15, 20, 25, 40, and 50 were added to the images, respectively, for a total of four remote sensing images.

Figure 14 shows the fused reconstructed remote sensing images of the above seven algorithm models, and the same from top to bottom part 1 shows six mixed noise images with impulse noise density of 0.001 and Gaussian noise levels of 10, 15, 20, 25, 40, 50, and part 2 to part 8 shows the reconstructed remote sensing images of BM3D, DnCNN, FFDNet, BM3D-DnCNN- Dual-PCNN, BM3D-FFDNet-Dual-PCNN, DnCNN-FFDNet-Dual-PCNN and the reconstructed remote sensing images of the method in this paper, respectively.

From the red box in the image, we can see that the method performs well for complex details, especially in the river area, and can effectively preserve the texture after image reconstruction, and the detailed contour reconstruction effect is better, and the comparison with other methods shows that the method has higher clarity, more complete contour structure, and higher sensitivity to the texture detail information in the image. From the green box of the image, it can be seen that the overall brightness of the image reconstructed by this method is higher, the high-frequency energy information is richly retained, and the parallax contrast effect is better. For example, in the green box, there is a big difference in height between the mountain top and the mountain pass in the mountain range area, and there is a big difference between the pixels of the image, which can be intuitively felt by the algorithm of this paper, and the visual effect is the best, which

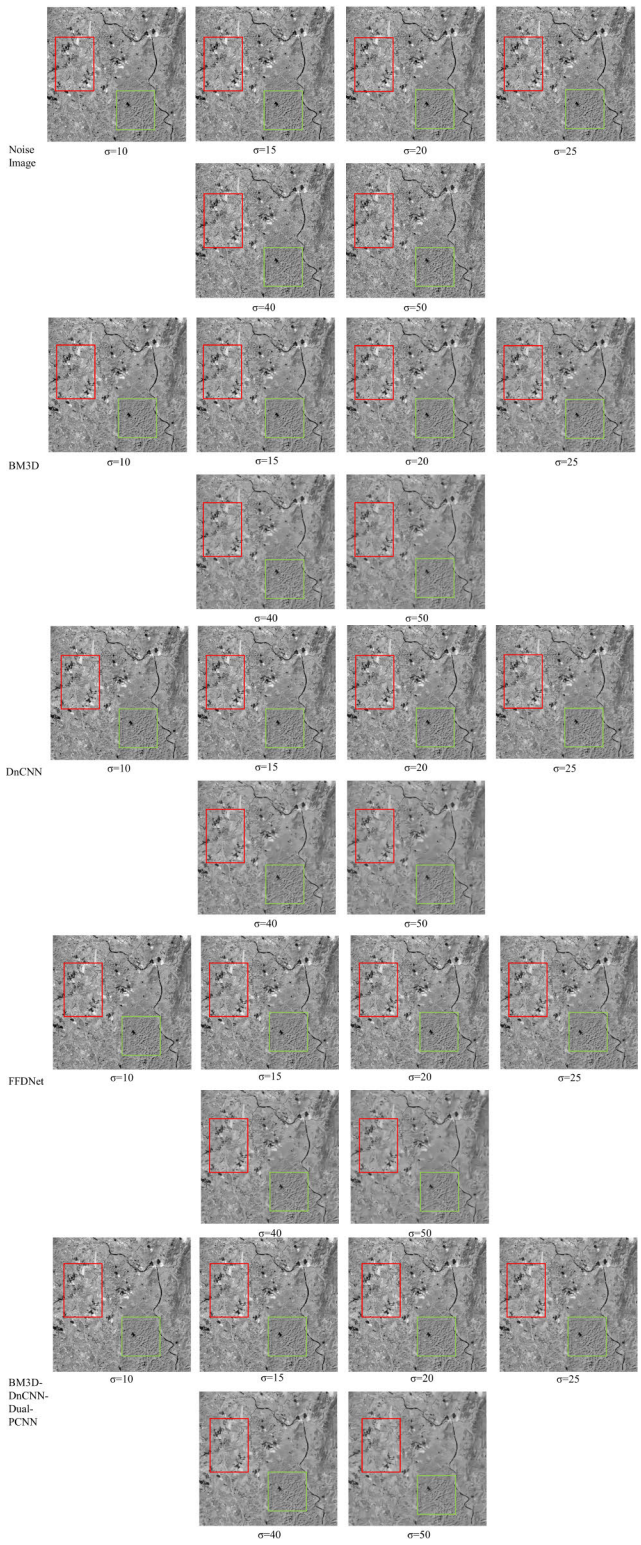

FIGURE 14. Remote sensing image rebuilding results by different methods on Mixed noise.

provides effective help for visual interpretation of remote sensing images.

Table 3 shows that the method in this paper has the best results among the compared algorithms in PSNR, SSIM, and

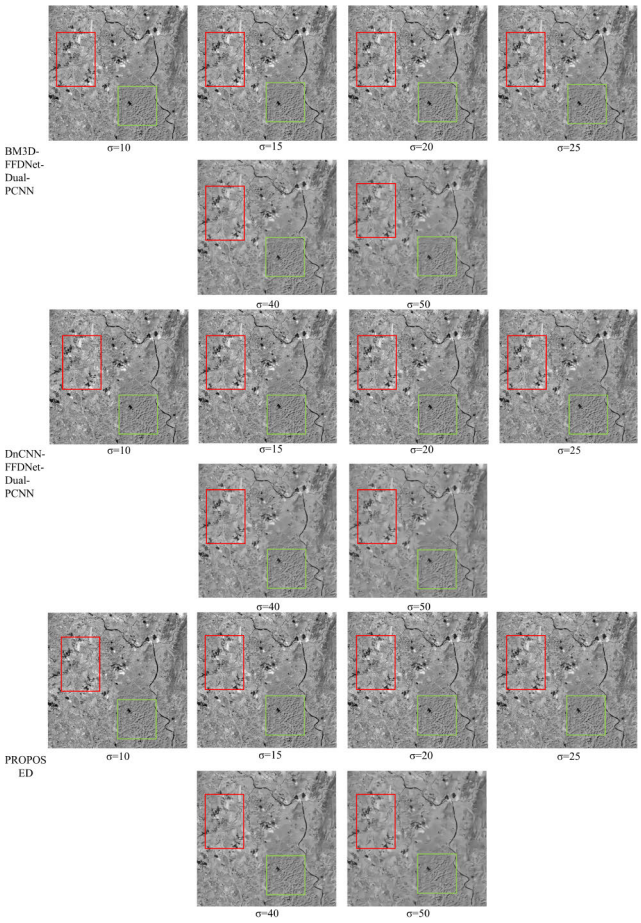

FIGURE 14. *(Continued.)* Remote sensing image rebuilding results by different methods on Mixed noise.

EPI, and a few cases are sub-optimal values, which once again verifies the excellent performance of the method in improving image sharpness, preserving texture details, and highlighting edge contour structures, thanks to the enhancement of image details by guided filtering and the effective separation enhancement of high-frequency sub-bands by NSCT, and at the same time can be compared with This is attributed to the enhanced image detail by guided filtering and the effective separation enhancement of high-frequency sub-bands by NSCT, and can be verified with the reconstructed remote sensing images of each method in Figure 14. One of the highlights of this method is that compared with DnCNN and FFDNet, which have very good performance in the field of image noise reduction, there is a breakthrough in both PSNR and SSIM, especially in Figure 13, we can see a very obvious improvement in PSNR, which indicates that the reconstruction method in this article is outstanding in image noise reduction.

The AG, SF, and EN of this paper are the best among all algorithms in Table 4. The AG and SF indicate that the remote sensing image is clearer, and the EN indicates that the remote sensing image itself has high information content. Therefore, it shows that the fusion reconstruction of remote

TABLE 3. Experimental results: the evaluation index of PSNR(dB), SSIM, EPI with pulse noise density 0.001 and gaussian noise level.

Method	10	15	20	25	40	50
	30.01	28.07	26.75	25.71	23.41	22.14
BM3D	0.901	0.837	0.778	0.725	0.583	**0.491**
	0.826	0.704	0.613	0.546	0.392	**0.284**
	30.21	28.34	27.08	26.05	23.58	22.16
DnCNN	**0.910**	0.855	0.804	0.756	0.594	0.479
	0.845	0.769	0.705	0.653	0.419	0.271
	30.20	28.35	**27.11**	26.08	23.65	22.18
FFDNet	0.909	0.855	0.805	0.757	0.601	0.479
	0.841	0.768	0.708	0.651	0.426	0.268
	30.09	28.14	26.87	25.80	23.51	22.20
BM3D-DnCNN-	0.906	0.840	0.788	0.732	0.588	0.486
Dual-PCNN	0.832	0.719	0.649	0.572	0.409	0.284
	30.04	28.18	26.86	25.84	23.53	22.20
BM3D-FFDNet-	0.903	0.845	0.787	0.737	0.591	0.485
Dual-PCNN	0.825	0.733	0.646	0.586	0.411	0.283
	30.21	28.35	27.10	26.06	23.63	22.18
DnCNN-FFDNet-	0.908	0.854	0.804	0.756	0.598	0.478
Dual-PCNN	0.846	0.766	0.705	0.649	0.422	0.268
	30.22	**28.36**	27.10	**26.08**	**23.67**	**22.20**
PROPOSED	0.909	**0.856**	**0.806**	**0.760**	**0.602**	0.483
	0.860	**0.800**	**0.729**	**0.681**	**0.441**	0.280

TABLE 4. Experimental results: the evaluation index of AG, SF, EN with pulse noise density 0.001 and gaussian noise.

Method	10	15	20	25	40	50
	9.29	8.28	7.43	6.76	5.01	**3.77**
BM3D	22.42	19.57	17.20	15.33	11.14	7.89
	6.94	6.89	6.84	6.80	6.61	**6.42**
	9.58	8.97	8.32	7.81	5.24	3.53
DnCNN	22.93	21.06	19.38	18.08	12.41	8.65
	6.95	6.92	6.88	6.85	6.61	6.37
	9.57	8.96	8.38	7.82	5.39	3.53
FFDNet	22.91	21.01	19.48	17.98	12.36	8.42
	6.95	6.91	6.88	6.85	6.62	6.38
	9.40	8.42	7.76	6.98	5.13	3.69
BM3D-DnCNN-	22.56	19.97	18.09	16.14	11.71	8.21
Dual-PCNN	6.94	6.90	6.87	6.81	6.62	6.41
	9.31	8.58	7.73	7.13	5.18	3.69
BM3D-FFDNet-	22.41	20.23	18.02	16.36	11.66	8.11
Dual-PCNN	6.93	6.91	6.86	6.82	6.62	6.41
	9.57	8.94	8.34	7.80	5.31	3.50
DnCNN-FFDNet	22.88	21.04	19.41	17.95	12.36	8.48
-Dual-PCNN	6.95	6.91	6.88	6.84	6.61	6.36
	9.71	**9.27**	**8.57**	**8.10**	**5.47**	3.60
PROPOSED	**23.25**	**21.76**	**19.96**	**18.70**	**12.84**	**8.83**
	6.96	**6.93**	**6.89**	**6.86**	**6.63**	6.37

sensing images by Dual-PCNN in the NSCT domain is more adequate in retaining spatial information, richer in energy information, and better in intuitive visual perception, which fully indicates the excellent quality of remote sensing image fusion.

As the noise level increases, the effect of this algorithm is very good at different levels in the normal noise range, but after the Gaussian noise reaches 50, the effect decreases in the extreme noise case. The reason for this is that the denoising ability of DnCNN and FFDNet for high-density Gaussian noise still needs to be improved, but the reconstruction ability of this algorithm for image details is still trustworthy in the non-extreme noise case.

In conclusion, after passing the grayscale image reconstruction experiment and remote sensing image fusion reconstruction experiment, a total of six quantitative evaluation indexes of two different types and subjective visual observation are integrated, and the reconstructed images are characterized by clear texture details, high-frequency edge contours, and rich spatial energy information, indicating that the method in this paper achieves excellent performance in noise reduction and fusion reconstruction of remote sensing images under complex noise conditions, with better Robustness [49], universality and excellence.

C. OTHER EXPERIMENT

In order to fully verify the generalizability of the method in different datasets of this paper, four images with pixel sizes of 256×256 and 512×512 in the Set12 dataset are selected for experiments. Also, add impulse noise with a density of

TABLE 5. Experimental results: the evaluation index of PSNR(dB), SSIM, EPI, AG, SF, EN with pulse noise density 0.001 and gaussian noise level 20.

Method	House	Butterfly	Parrot	Couple
BM3D	33.78/0.873/**0.633**	30.29/0.920/**0.870**	27.41/0.847/0.698	30.18/0.836/0.647
	3.51/13.12/**6.35**	8.03/24.01/**7.42**	6.26/24.00/**7.46**	5.27/15.34/7.35
DnCNN	33.92/0.872/0.595	31.38/0.934/0.831	**27.66**/0.853/0.699	30.47/0.842/0.654
	3.41/13.66/6.26	7.82/25.62/7.38	6.29/24.74/7.38	5.35/16.04/7.35
FFDNet	**34.10**/0.873/0.579	31.36/0.934/0.826	27.65/0.854/0.697	30.60/0.847/0.654
	3.36/13.57/6.20	7.82/25.26/7.38	6.29/24.92/7.38	5.39/16.03/7.35
BM3D-DnCNN-Dual-PCNN	33.86/0.874/0.611	30.80/0.926/0.870	27.41/0.853/0.697	30.29/0.839/0.661
	3.45/13.38/6.27	**8.04**/25.01/7.41	6.25/24.31/7.42	5.36/15.78/7.36
BM3D-FFDNet-Dual-PCNN	33.97/**0.875**/0.600	30.81/0.927/0.860	27.39/0.854/0.691	30.35/0.842/0.651
	3.41/13.34/6.22	7.99/24.73/7.40	6.22/24.30/7.41	5.32/15.65/7.35
DnCNN-FFDNet-Dual-PCNN	34.03/0.873/0.586	31.39/0.934/0.832	27.61/0.854/0.697	30.58/0.846/0.654
	3.37/13.62/6.22	7.85/25.52/7.39	6.29/24.83/7.38	5.38/16.04/7.35
PROPOSED	34.01/0.873/0.619	**31.41/0.935**/0.855	27.63/**0.854/0.724**	**30.58/0.848/0.692**
	3.48/13.95/6.24	7.99/**26.07**/7.40	**6.45/ 25.31**/7.39	**5.60/16.68/7.36**

0.001 and Gaussian noise with a noise level of 20 to each image respectively for the experiments.

Figure 15 shows the reconstruction effects of the above seven algorithm models in four images, the same image from left to right in the first row is the original image, noisy image, BM3D, DnCNN, FFDNet reconstructed image, and the second row from left to right is divided into BM3D-DnCNN-Dual-PCNN, BM3D-FFDNet-Dual-PCNN, DnCNN- FFDNet-Dual-PCNN and the reconstruction effect of the method in this paper. The red frame is the zoomed image of the blue frame, and we can clearly observe that the texture information of this method is richer than other algorithms, and it is also more consistent with the human eye visual observation.

From Table 5, it is found that the six indexes of PSNR, SSIM, EPI, AG, SF, and EN are optimal or suboptimal solutions on all four images, which can illustrate the effectiveness of this paper's algorithm. At the same time, it can be observed that on the House image with a simple image structure, some of the index results are not optimal, but after the image structure becomes complex, instead, the performance of this paper's algorithm becomes more excellent, and on the Couple image with the most complex structure, all indexes of this paper's algorithm are optimal, which can show that this paper's algorithm has very good results for the extraction and retention of complex texture information features. In summary, this algorithm has certain generalization abilities in different fields and different data sets.

D. ABLATION STUDY

To fully consider the importance of each module in the method, an Ablation Study is performed. the following cases are mainly considered: (a) missing IMFLED Module, (b) missing DnCNN and FFDNet Module, (c) missing GUIDED Module, (d) missing Dual-PCNN Module, (e) Missing GUIDED and Dual-PCNN Module. the experimental results are shown in Figure 16 and each evaluation metric is shown in Table 6.

In the absence of the Impulse Noise and Gaussian Noise removal modules, the impact on the image quality is very significant, and therefore the metrics are less informative. In the absence of GUIDED Medule and Dual-PCNN Medule, a significant gap can be found in the metrics other than PSNR and EN values. The method in this paper enhances the image texture details and capability information while maintaining efficient noise reduction.

Besides, in this paper, different SOTA image fusion algorithms are chosen for the ablation study, the noise preprocessing module is kept and only the fusion module is replaced to verify the effectiveness of the image fusion module in this paper. In the literature [50], a new multimodal medical image fusion method in the non-subsampled shearlet transform (NSST) domain is proposed for the high-frequency subband using a parameter-adaptive pulse-coupled neural network (PA-PCNN) model. In the literature [51], a novel multimodal medical image fusion algorithm is proposed, incorporating boundary measurement pulse-coupled neural network and energy properties. The same metrics mentioned above were used for validation and the results are shown in Table 7.

From the Table 7, all the metrics are found to be optimal, which fully illustrates the excellent performance of the image fusion module in the algorithm of this paper. In summary, the experiments in this chapter show to a certain extent that the modules in the algorithm play an important role in the operation of the overall algorithm.

V. DISCUSSIONS

A. DEAL WITH IMPULSE AND GAUSSIAN MIXED NOISE

For impulsive noise, CNN-based models cannot be effective, but excellent for Gaussian noise, while IMFLED can efficiently identify impulsive noise and has better capability compared to other algorithms for removing impulsive noise. Therefore, IMFLED is selected to remove composite noise jointly with DnCNN and FFDNet to obtain excellent results.

The reconstructed image in this article has better performance in PSNR, SSIM, EPI metrics, higher image sharpness, fuller texture information, and more complete edge contour structure compared with the current state-of-the-art two types of noise reduction algorithms such as BM3D, DnCNN, and FFDNet. Therefore, the method in this article can also be

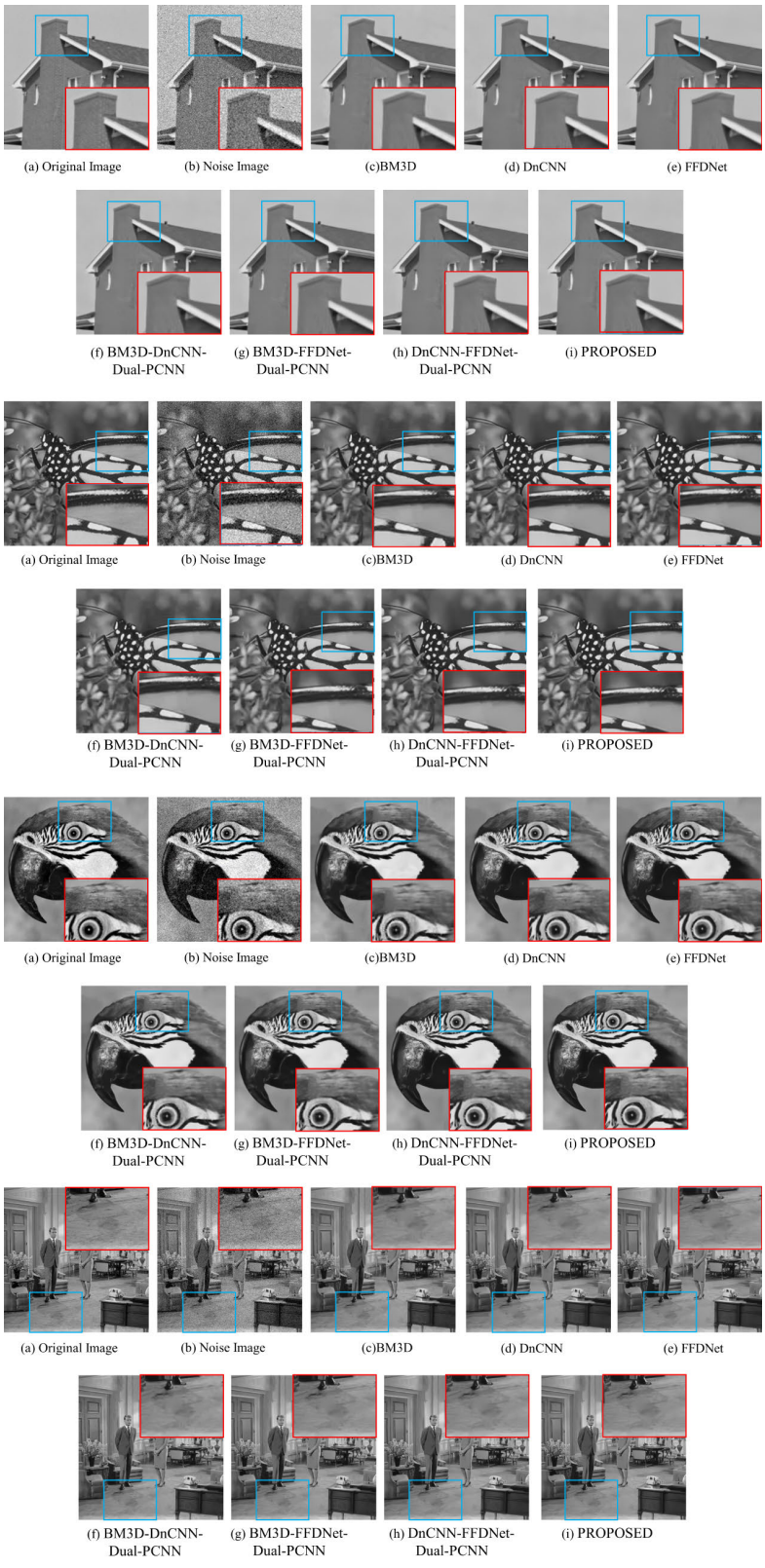

(a) Original Image (b) Noise Image (c)BM3D (d) DnCNN (e) FFDNet

(f) BM3D-DnCNN-Dual-PCNN (g) BM3D-FFDNet-Dual-PCNN (h) DnCNN-FFDNet-Dual-PCNN (i) PROPOSED

(a) Original Image (b) Noise Image (c)BM3D (d) DnCNN (e) FFDNet

(f) BM3D-DnCNN-Dual-PCNN (g) BM3D-FFDNet-Dual-PCNN (h) DnCNN-FFDNet-Dual-PCNN (i) PROPOSED

(a) Original Image (b) Noise Image (c)BM3D (d) DnCNN (e) FFDNet

(f) BM3D-DnCNN-Dual-PCNN (g) BM3D-FFDNet-Dual-PCNN (h) DnCNN-FFDNet-Dual-PCNN (i) PROPOSED

(a) Original Image (b) Noise Image (c)BM3D (d) DnCNN (e) FFDNet

(f) BM3D-DnCNN-Dual-PCNN (g) BM3D-FFDNet-Dual-PCNN (h) DnCNN-FFDNet-Dual-PCNN (i) PROPOSED

FIGURE 15. Set12 dataset image rebuilding results by different methods on Mixed noise.

applied as an excellent image noise reduction method in other multi-type hybrid noise reduction fields in the future.

The limitation is that it is difficult to apply directly by DnCNN and FFDNet for unknown levels of noise in the

TABLE 6. Experimental results: the evaluation index of PSNR(dB), SSIM, EPI, AG, SF, EN with the Couple images in the Set12 dataset.

Method	PSNR	SSIM	EPI	AG	SF	EN
NO IMFLED	30.39	0.841	0.737	5.86	17.79	7.39
NO DnCNN+FFDNET	22.09	0.452	3.000	14.99	43.99	7.58
NO GUIDED	30.57	0.847	0.680	5.50	16.44	7.35
NO Dual-PCNN	30.58	0.846	0.663	5.46	16.26	7.35
NO GUIDED+Dual-PCNN	30.58	0.847	0.681	5.51	16.45	7.35
PROPOSED	30.58	0.848	0.692	5.60	16.68	7.36

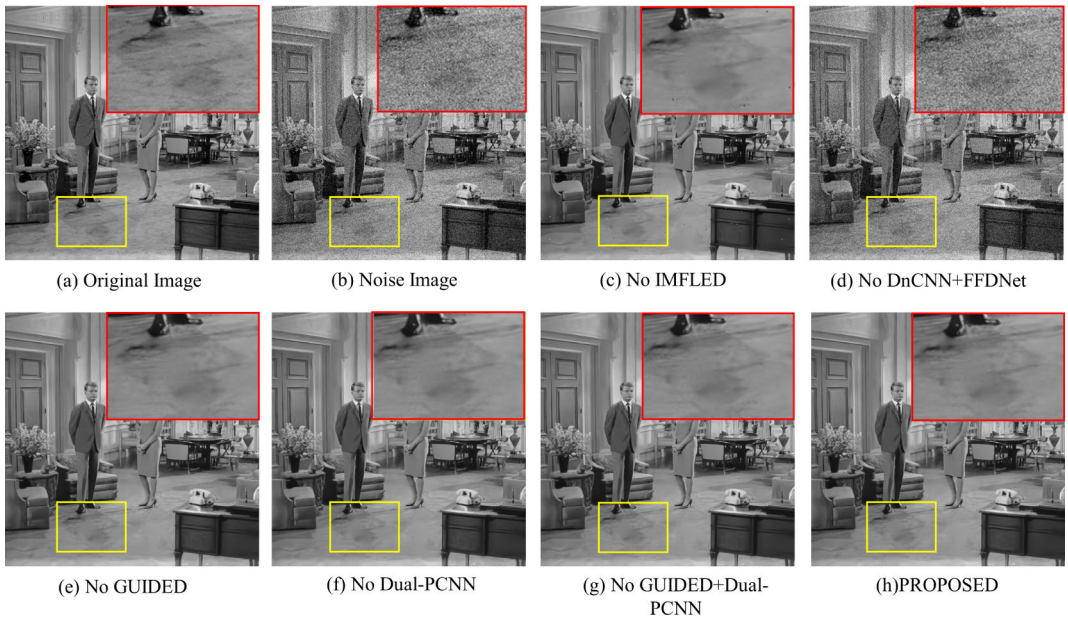

(a) Original Image (b) Noise Image (c) No IMFLED (d) No DnCNN+FFDNet

(e) No GUIDED (f) No Dual-PCNN (g) No GUIDED+Dual-PCNN (h)PROPOSED

FIGURE 16. The results of ablation experiments.

TABLE 7. Experimental results: the evaluation index of PSNR (dB), SSIM, EPI with pulse noise density 0.001 and gaussian noise level 20 (Comparison with SOTA method).

Method	House	Butterfly	Parrot	Couple
NSST-PAPCNN	33.94/0.872/0.597	31.39/0.934/0.833	**27.66**/0.853/0.701	30.51/0.844/0.659
	3.41/13.68/**6.26**	7.83/25.64/7.38	6.31/24.79/7.38	5.38/16.09/7.35
NSST-MSMG-PCNN	33.98/0.872/0.605	31.40/0.934/0.836	27.66/0.854/0.708	30.55/0.845/0.668
	3.43/13.73/6.26	7.85/25.69/7.38	6.33/24.94/7.38	5.44/16.22/7.35
PROPOSED	**34.00/0.873/0.618**	**31.41/0.935/0.855**	27.64/**0.854/0.725**	**30.58/0.846/0.692**
	3.48/13.95/6.24	**7.99/26.07/7.40**	**6.45/25.31/7.39**	**5.60/16.68/7.36**

real world, both of which need to know the noise level to achieve the best results. For example, FFDNet needs to provide the exact noise level to fit the model when denoising. Therefore, the introduction of noise level estimation methods or noise blind denoising by generating adversarial networks is considered in the subsequent studies. While DnCNN and FFDNet, as two deep learning denoising models, have limited generalization ability with their effectiveness on images in the real world yet to be verified.

B. IMAGE FUSION AND RECONSTRUCTION

Both NSCT and PCNN can be used for image fusion alone or jointly for image fusion to achieve better results. In this article, the method provides basic information for image fusion by using the guided filter to stimulate low-frequency sub-bands in the NSCT domain and enrich the sub-band texture information. After analyzing the guided filtering of the detail layer image, it is found that it has high structural similarity with the unidirectional high-frequency sub-bands of NSCT, and the detail layer is richer in high-frequency information. Therefore, after enhancing the detail layer image by magnification coefficient, it is fused with the high- frequency sub-bands with high structural similarity to enrich the high-frequency information and make the contour structure more complete.

The NSCT reconstructed images using simplified parametric adaptive Dual-PCNN to fuse each information-enhanced sub-band showed excellent performance in terms of AG, SF, and EN indexes, indicating high image information content and rich spatial energy retention. Therefore, the sub-band

fusion rules in this research method, and the simplified parametric adaptive Dual-PCNN model have excellent image fusion capability.

The limitation lies in how to ensure the continuous correlation between sub-bands in multi-scale decomposition, and the spectral characteristics of optical remote sensing images should be paid attention to in the subsequent research. Meanwhile, remote sensing images are large-scale images, and the algorithm of this paper needs to improve its operational efficiency when reproducing them in the real world.

VI. CONCLUSION

To address the problem that the existing methods cannot effectively preserve the image energy texture details and highlight the edge contour structure while reducing noise in the case of optical remote sensing images with composite noise, a method is proposed to enhance the multi-source image frequency sub-bands with noise reduction by DnCNN and FFDNet in NSCT domain using the guided filter, and then reconstruct them by fusion with simplified parametric adaptive Dual-PCNN. In this article, we combine the advantages of IMFLED and CNN for noise identification and the advantages of NSCT domain and PCNN for image fusion and incorporate the improved guided filter for excellent image detail stimulation. After the experimental validation with grayscale images and optical remote sensing images, excellent results are achieved in the evaluation of different types of quantitative indexes, indicating the superiority of this research method in image noise reduction and reconstruction.

The limitations of this article are the inadequate adaptive selection of parameters and sub-band enhancement coefficients for the guided filter, the need to reduce the halo artifacts caused by mutual interference of edge pixels, and the combination of multi-scale multi-feature image information fusion sub-band to improve image quality are the future target research directions.In our future research, we will focus on the reconstruction of remote sensing image information from different satellite sources and different resolutions, and apply the adversarial neural network in deep learning to the reconstruction of remote sensing image information as well as focus on the 3D reconstruction of remote sensing images [52]. Besides, we also focus on applying the research methods proposed in this paper to the research of noise reduction and fusion reconstruction of multimodal medical images, visible and infrared light images, and multi-focus images.

REFERENCES

[1] U. Shafi, R. Mumtaz, N. Iqbal, S. M. H. Zaidi, S. A. R. Zaidi, I. Hussain, and Z. Mahmood, "A multi-modal approach for crop health mapping using low altitude remote sensing, Internet of Things (IoT) and machine learning," *IEEE Access*, vol. 8, pp. 112708–112724, 2020.

[2] L. Zheng and W. Xu, "An improved adaptive spatial preprocessing method for remote sensing images," *Sensors*, vol. 21, no. 17, p. 5684, Aug. 2021.

[3] K. Dabov, A. Foi, V. Katkovnik, and K. Egiazarian, "Image denoising by sparse 3-D transform-domain collaborative filtering," *IEEE Trans. Image Process.*, vol. 16, no. 8, pp. 2080–2095, Aug. 2007.

[4] E. Candès and B. Recht, "Exact matrix completion via convex optimization," *Commun. ACM*, vol. 55, no. 6, pp. 111–119, Jun. 2012.

[5] S. Gu, L. Zhang, W. Zuo, and X. Feng, "Weighted nuclear norm minimization with application to image denoising," in *Proc. IEEE Conf. Comput. Vis. Pattern Recognit.*, Jun. 2014, pp. 2862–2869.

[6] K. Zhang, W. Zuo, Y. Chen, D. Meng, and L. Zhang, "Beyond a Gaussian denoiser: Residual learning of deep CNN for image denoising," *IEEE Trans. Image Process.*, vol. 26, no. 7, pp. 3142–3155, Jul. 2017.

[7] K. Zhang, W. Zuo, and L. Zhang, "FFDNet: Toward a fast and flexible solution for CNN-based image denoising," *IEEE Trans. Image Process.*, vol. 27, no. 9, pp. 4608–4622, Sep. 2018.

[8] S. Chen, D. Shi, M. Sadiq, and X. Cheng, "Image denoising with generative adversarial networks and its application to cell image enhancement," *IEEE Access*, vol. 8, pp. 82819–82831, 2020.

[9] A. Khan, W. Jin, and R. A. Naqvi, "Perceptual adversarial non-residual learning for blind image denoising," *Soft Comput.*, vol. 26, no. 16, pp. 7933–7957, Mar. 2022.

[10] Y. Pan, C. Ren, X. Wu, J. Huang, and X. He, "Real image denoising via guided residual estimation and noise correction," *IEEE Trans. Circuits Syst. Video Technol.*, vol. 33, no. 4, pp. 1994–2000, Apr. 2023.

[11] R. Vijayarajan and S. Muttan, "Discrete wavelet transform based principal component averaging fusion for medical images," *AEU-Int. J. Electron. Commun.*, vol. 69, no. 6, pp. 896–902, Jun. 2015.

[12] Y. Kong, F. Hong, H. Leung, and X. Peng, "A fusion method of optical image and SAR image based on dense-UGAN and Gram–Schmidt transformation," *Remote Sens.*, vol. 13, no. 21, p. 4274, Oct. 2021.

[13] R. Srivastava and A. Khare, "Multifocus noisy image fusion using contourlet transform," *Imag. Sci. J.*, vol. 63, no. 7, pp. 408–422, Jul. 2015.

[14] A. L. Da Cunha, J. Zhou, and M. N. Do, "The nonsubsampled contourlet transform: Theory, design, and applications," *IEEE Trans. Image Process.*, vol. 15, no. 10, pp. 3089–3101, Oct. 2006.

[15] G. Bhatnagar, Q. M. J. Wu, and Z. Liu, "Directive contrast based multimodal medical image fusion in NSCT domain," *IEEE Trans. Multimedia*, vol. 15, no. 5, pp. 1014–1024, Aug. 2013.

[16] L. Li, H. Ma, and Z. Jia, "Multiscale geometric analysis fusion-based unsupervised change detection in remote sensing images via FLICM model," *Entropy*, vol. 24, no. 2, p. 291, Feb. 2022.

[17] Y. Li and J. Zhao, "A novel medical image fusion method using multi-channel pulse coupled neural networks," *IEEE Access*, vol. 8, pp. 157572–157586, 2020.

[18] X. Ma, Z. Wang, S. Hu, and S. Kan, "Multi-focus image fusion based on multi-scale generative adversarial network," *Entropy*, vol. 24, no. 5, p. 582, Apr. 2022.

[19] R. Eckhorn, H. J. Reitboeck, M. Arndt, and P. Dicke, "Feature linking via synchronization among distributed assemblies: Simulations of results from cat visual cortex," *Neural Comput.*, vol. 2, no. 3, pp. 293–307, Sep. 1990.

[20] Y. Chen, S.-K. Park, Y. Ma, and R. Ala, "A new automatic parameter setting method of a simplified PCNN for image segmentation," *IEEE Trans. Neural Netw.*, vol. 22, no. 6, pp. 880–892, Jun. 2011.

[21] X. Wang, Z. Li, H. Kang, Y. Huang, and D. Gai, "Medical image segmentation using PCNN based on multi-feature grey wolf optimizer bionic algorithm," *J. Bionic Eng.*, vol. 18, no. 3, pp. 711–720, Jun. 2021.

[22] C. Panigrahy, A. Seal, and N. K. Mahato, "Fractal dimension based parameter adaptive dual channel PCNN for multi-focus image fusion," *Opt. Lasers Eng.*, vol. 133, Oct. 2020, Art. no. 106141.

[23] C. Panigrahy, A. Seal, and N. K. Mahato, "Parameter adaptive unit-linking dual-channel PCNN based infrared and visible image fusion," *Neurocomputing*, vol. 514, pp. 21–38, Dec. 2022.

[24] C. Panigrahy, A. Seal, C. Gonzalo-Martín, P. Pathak, and A. S. Jalal, "Parameter adaptive unit-linking pulse coupled neural network based MRI-PET/SPECT image fusion," *Biomed. Signal Process. Control*, vol. 83, May 2023, Art. no. 104659.

[25] G. Sahu, A. Seal, D. Bhattacharjee, R. Frischer, and O. Krejcar, "A novel parameter adaptive dual channel MSPCNN based single image dehazing for intelligent transportation systems," *IEEE Trans. Intell. Transp. Syst.*, vol. 24, no. 3, pp. 3027–3047, Mar. 2023.

[26] B. Cheng, L. Jin, and G. Li, "Infrared and visual image fusion using LNSST and an adaptive dual-channel PCNN with triple-linking strength," *Neurocomputing*, vol. 310, pp. 135–147, Oct. 2018.

[27] X. Feng, W. Zhang, X. Su, and Z. Xu, "Optical remote sensing image denoising and super-resolution reconstructing using optimized generative network in wavelet transform domain," *Remote Sens.*, vol. 13, no. 9, p. 1858, May 2021.

[28] Q. Yanfeng, "New effective filtering algorithm for the removal of impulse noise from images," *J. Comput.-Aided Des. Comput. Graph.*, vol. 15, no. 4, pp. 397–401, Apr. 2003.
[29] K. He, J. Sun, and X. Tang, "Guided image filtering," *IEEE Trans. Pattern Anal. Mach. Intell.*, vol. 35, no. 6, pp. 1397–1409, Jun. 2013.
[30] O. Abdel-Hamid, A.-R. Mohamed, H. Jiang, L. Deng, G. Penn, and D. Yu, "Convolutional neural networks for speech recognition," *IEEE/ACM Trans. Audio, Speech, Language Process.*, vol. 22, no. 10, pp. 1533–1545, Oct. 2014.
[31] S. Ioffe and C. Szegedy, "Batch normalization: Accelerating deep network training by reducing internal covariate shift," in *Proc. Int. Conf. Mach. Learn. (PMLR)*, 2015, pp. 448–456.
[32] C. Tomasi and R. Manduchi, "Bilateral filtering for gray and color images," in *Proc. 6th Int. Conf. Comput. Vis.*, Jan. 1998, pp. 839–846.
[33] J. Jeon, J. Kim, K. Lee, S. Oh, and J. Ok, "Gradient inversion with generative image prior," in *Proc. Adv. neural Inf. Process. Syst.*, vol. 34, May 2021, pp. 29898–29908.
[34] L. Chen, Z. Chen, R. K. Singh, R. V. Vinu, and J. Pu, "Increasing field of view and signal to noise ratio in the quantitative phase imaging with phase shifting holography based on the Hanbury Brown-Twiss approach," *Opt. Lasers Eng.*, vol. 148, Jan. 2022, Art. no. 106771.
[35] A. L. M. Levada, "Closed-form Bayesian image denoising: Improving the adaptive Wiener filter through pairwise Gaussian–Markov random fields," *Commun. Statist. Simul. Comput.*, vol. 50, no. 4, pp. 1094–1118, Apr. 2021.
[36] T. Vaiyapuri, H. Alaskar, Z. Sbai, and S. Devi, "GA-based multi-objective optimization technique for medical image denoising in wavelet domain," *J. Intell. Fuzzy Syst.*, vol. 41, no. 1, pp. 1575–1588, Aug. 2021.
[37] X. Liao and M. Feng, "Time-fractional diffusion equation-based image denoising model," *Nonlinear Dyn.*, vol. 103, no. 2, pp. 1999–2017, Jan. 2021.
[38] A. A. Yahya, J. Tan, B. Su, M. Hu, Y. Wang, K. Liu, and A. N. Hadi, "BM3D image denoising algorithm based on an adaptive filtering," *Multimedia Tools Appl.*, vol. 79, nos. 27–28, pp. 20391–20427, Apr. 2020.
[39] T. Remez, O. Litany, R. Giryes, and A. M. Bronstein, "Class-aware fully convolutional Gaussian and Poisson denoising," *IEEE Trans. Image Process.*, vol. 27, no. 11, pp. 5707–5722, Nov. 2018.
[40] H. Yin, Y. Gong, and G. Qiu, "Side window guided filtering," *Signal Process.*, vol. 165, pp. 315–330, Dec. 2019.
[41] P. J. Thomas, R. S. Allison, P. Carr, E. Shen, S. Jennings, T. Macuda, G. Craig, and R. Hornsey, "Physical modeling and characterization of the halo phenomenon in night vision goggles," *Proc. SPIE*, vol. 5800, pp. 21–31, May 2005.
[42] A. Saadia and A. Rashdi, "Incorporating fractional calculus in echo-cardiographic image denoising," *Comput. Electr. Eng.*, vol. 67, pp. 134–144, Apr. 2018.
[43] Y. Liu, X. Chen, H. Peng, and Z. Wang, "Multi-focus image fusion with a deep convolutional neural network," *Inf. Fusion*, vol. 36, pp. 191–207, Jul. 2017.
[44] P. Chai, X. Luo, and Z. Zhang, "Image fusion using quaternion wavelet transform and multiple features," *IEEE Access*, vol. 5, pp. 6724–6734, 2017.
[45] X. Qin, Y. Ban, P. Wu, B. Yang, S. Liu, L. Yin, M. Liu, and W. Zheng, "Improved image fusion method based on sparse decomposition," *Electronics*, vol. 11, no. 15, p. 2321, Jul. 2022.
[46] P. Arbeláez, M. Maire, C. Fowlkes, and J. Malik, "Contour detection and hierarchical image segmentation," *IEEE Trans. Pattern Anal. Mach. Intell.*, vol. 33, no. 5, pp. 898–916, May 2011.
[47] Y. Han, B. Tang, and L. Deng, "An enhanced convolutional neural network with enlarged receptive fields for fault diagnosis of planetary gearboxes," *Comput. Ind.*, vol. 107, pp. 50–58, May 2019.
[48] C. Yan, Z. Li, Y. Zhang, Y. Liu, X. Ji, and Y. Zhang, "Depth image denoising using nuclear norm and learning graph model," *ACM Trans. Multimedia Comput., Commun., Appl.*, vol. 16, no. 4, pp. 1–17, Nov. 2020.
[49] C. Xie, Y. Wu, L. van der Maaten, A. L. Yuille, and K. He, "Feature denoising for improving adversarial robustness," in *Proc. IEEE/CVF Conf. Comput. Vis. Pattern Recognit. (CVPR)*, Jun. 2019, pp. 501–509.
[50] M. Yin, X. Liu, Y. Liu, and X. Chen, "Medical image fusion with parameter-adaptive pulse coupled neural network in nonsubsampled shearlet transform domain," *IEEE Trans. Instrum. Meas.*, vol. 68, no. 1, pp. 49–64, Jan. 2019.
[51] W. Tan, P. Tiwari, H. M. Pandey, C. Moreira, and A. K. Jaiswal, "Multimodal medical image fusion algorithm in the era of big data," *Neural Comput. Appl.*, pp. 1–21, Jul. 2020.
[52] Z. Qi, Z. Zou, H. Chen, and Z. Shi, "3D reconstruction of remote sensing mountain areas with TSDF-based neural networks," *Remote Sens.*, vol. 14, no. 17, p. 4333, Sep. 2022.

PENGCHENG HU received the B.E. degree in computer science and technology from Chongqing Jiaotong University, China, in 2020. He is currently pursuing the master's degree in surveying and mapping science and technology with the Guilin University of Technology, China. He has authored or coauthored several papers on image processing, photogrammetric data processing, and other research areas. His main research interests include computer vision, image fusion, and photogrammetry data processing and applications.

SHIHUA TANG received the Ph.D. degree. He is currently a Professor and a Master's Supervisor. He is mainly engaged in the research of automatic acquisition and processing of surveying and mapping data and the application development of measurement robots, the theory and hardware development related to automatic mapping, GPS application research, software integration, and related development. He has presided over five Guangxi funds and national natural science funds, presided over and participated in the development of dozens of horizontal scientific research projects, published more than 50 academic papers in related fields, and obtained six national patents. He has won four provincial teaching excellence awards, three Guangxi science and technology awards, and three textbooks, such as *Digital Mapping*.

YAN ZHANG received the master's degree in surveying and mapping science and technology from the Guilin University of Technology. He is an Assistant Experimentalist. He is mainly engaged in GNSS data processing and application research.

XIAOHUI SONG received the B.E. degree in surveying and mapping engineering from the Xiamen Institute of Technology, China, in 2021. He is currently pursuing the master's degree in resources and environment with the Guilin University of Technology. His main research interests include UAV data processing and applications.

MENGBO SUN received the B.E. degree in geographic information science from the Nanning Institute of Technology, China, in 2022. She is currently pursuing the M.S. degree in resources and environment with the Guilin University of Technology. Her main research interests include inertial navigation and combined navigation.